

# FLOW PATTERNS AND MASS TRANSPORT IN A THREE DIMENSIONAL MODEL OF THE HUMAN LUNG

Katrin Bauer\*, Alexander Rudert\*, Willy Mattheus\*, Friederike Lindner\*, Christoph Brücker\*

\* Institute of Mechanics and Fluidynamics  
Lampadiusstr.2, 09599 Freiberg, Germany,  
katrin.bauer@imfd.tu-freiberg.de

## Abstract

The flow patterns occurring in the upper human airways were investigated at a realistic bronchial tree model which incorporates six bifurcating generations. The flow was investigated by means of computational fluid dynamics. Therefore, oscillatory flow at varying Reynolds and Womersley numbers was applied. Different flow conditions were simulated including normal ventilation as well as high frequency ventilation conditions. For validation of the numerical results, particle image velocimetry (PIV) measurements of the main branches are used. The numerical results were in good agreement with the PIV results. The numerical simulation then provides information about the flow patterns in the lower branches and the variation at different tidal volumes and ventilation frequencies. Furthermore, the three-dimensional structure of emerging secondary flows was analyzed. The secondary vortices strongly depend on local curvature but are not influenced by upstream flow or geometry, respectively.

**Keywords:** Lung, airways, numerical simulation, 3D model, secondary flows, mass transport, flow patterns.

## Introduction

For patients with severely injured lungs mechanical ventilation can be a life saving treatment. However, as applied over a longer period of time, ventilator induced lung injuries may occur. Therefore, improved methods of ventilation, so called 'protective ventilation' should be applied. The first step of an improved ventilation strategy is a comprehensive understanding of the lung flow and mass transport under normal, healthy breathing conditions.

Therefore, a realistic, three-dimensional model of the bronchial tree has been generated. The model starts with the trachea and bifurcates down to the 6th generation. The geometry is based on data from Weibel [23] and Horsfield [11] as will be described in the subsequent section. Care was taken for model generation since a realistic geometry is crucial. In many studies the airway geometry is strongly simplified. Symmetric models have been frequently used (e.g. [9, 13, 18, 25]). The study from Liu et al. [17] has shown that especially symmetric geometry leads to asymmetric distribution of mass within the airways. Very frequently, only a single bifurcation model has been employed for simplicity [7, 10, 16, 20]. For a first impression of bifurcating flow behavior that should be sufficient. Typical flow patterns such as skewed velocity profiles [1] and secondary vortices could be shown already for these simple models. Since the impedance of the lower generations is missing, information about mass transport mechanisms into the lower branches as well as the impact of the lower

branches on the main airways remains unknown. Bauer and Brücker [2] have shown for a 6 generation model that, especially for higher Reynolds numbers, the influence of the branching geometry becomes more important. Different pressure losses dominate flow partitioning. The impact of different ventilation frequencies and tidal volumes (Reynolds numbers) on the flow patterns, especially in the lower generation was investigated in the study presented here. Therefore, numerical methods were employed using the open source code OpenFoam V.1.51 dev. The three-dimensional structure of the emerging secondary flow occurring in the human lung airways will be further investigated in detail. So far, secondary structures in the human lung have been extensively investigated by Fresconi and Prasad [9]. However, their findings were restricted to 2D, planar measurements. They have presented the vortex development during one breathing cycle and for different Reynolds numbers.

## Numerical model

### *Mathematical model*

The governing equations for incompressible, unsteady fluid flow are the continuity equation and the Navier-Stokes-equations. In tensor notation they are

$$\frac{\partial u_i}{\partial x_i} = 0, \quad (1)$$

$$\frac{\partial u_i}{\partial t} + u_j \frac{\partial u_i}{\partial x_j} = -\frac{1}{\rho} \frac{\partial p}{\partial x_i} + \frac{\partial}{\partial x_j} \left( \nu \frac{\partial u_i}{\partial x_j} \right) + g_i, \quad (2)$$

where  $u_i$  and  $u_j$  are the components of the velocity vector,  $p$  is the pressure,  $\rho$  and  $\nu$  the fluid density and kinematic viscosity, respectively. Here, the Einstein summation is used so that the repeated index implies summation. Furthermore, an additional volume force is considered here which includes the gravity  $g$  since for comparison to the experimental results, the properties of the experimental liquid (water-glycerine) were invoked.

### Numerical Methods

For numerical simulation of the lung flow, the Finite Volume Method (FVM) was applied. Therefore, the equations 1 and 2 were integrated over a control volume and then discretized. The FVM requires a decomposition of the computational domain into grid cells. The discretization of the governing equations is invoked at the knots of the numerical grid. After discretization, a linear set of equations is received which are solved by the solver GAMG (Geometric Agglomerated algebraic MultiGrid solver) which is implemented in OpenFoam. This solver first coarsens the grid to approximate a fast starting solution for a finer grid [3]. All methods applied for numerical flow simulation are summarized in Tab. 1

**Table 1 Numerical methods for simulation of the lung flow.**

Mathematical operation	Numerical method
discretization of convective terms	Gauss upwind, 1st order
discretization of time derivatives	backward differencing
pressure-velocity coupling	PISO algorithm

The PISO algorithm mentioned in table 1 stands for Pressure Implicit with Splitting of Operators [22]) whereat two interpolation loops were employed, here. The iterations, necessary to calculate the solution of each time step, were stopped as a truncation error of  $10^{-8}$  was reached.

### Geometry

The geometry of the airway model is based on two different data sets. The radius of the curvature with its origin at the daughter branch (see. Tab. 2) as well as the transition zones between the parent and the daughter branches are based on Horsfield [11] data. For the diameters and lengths of the generations, data from Weibel [23] were taken which apply for an ideal bifurcation of the lung. In order to create an asymmetric geometry the branch lengths  $l_r$  and  $l_l$  in each bifurcation relate to each other according to the golden ratio with  $l_r/l_l \approx 1.62$ . The mean value of the branch length  $l = (l_r + l_l)/2$  in each bifurcation corresponds to the value given by Weibel. Each daughter bifurcation is connected to the parent branch by rotating the plane of the daughter branches by  $90^\circ$  with respect to the previous orientation. The only exception is the first generation which is connected to the trachea by a rotation angle of  $60^\circ$ . All geometrical data which were used for the

design of the lung model are summarized in Tab. 2. For reference, the variables used in Tab. 2 are presented in Fig. 1.

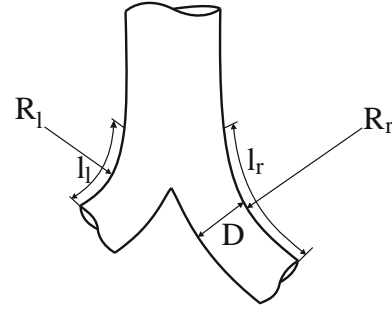


**Figure 1 Nomenclature of the bifurcations.**

**Table 2 Geometrical data of the lung model in mm.**

Gen.	D	$l_l$	$l_r$	$R_l$	$R_r$
0	18.0	150			
1	12.2	36.8	59.3	36.6	55.0
2	8.3	14.7	23.6	52.2	29.0
3	5.6	5.8	9.4	33.2	45.0
4	4.5	9.8	15.8	17.8	18.7
5	3.5	8.2	13.3	21.1	21.8
6	2.8	6.9	11.2	25.0	31.2

The model geometry was discretized by 1,926,391 tetrahedral cells which form an unstructured mesh. The mesh was created with ICEM CFD V.12 from ANSYS. Figure 2a) depicts the discretized lung model. The enlarged views show the grid structure of the inlet boundary with a diameter of 18 mm (Fig. 2b)) and one of the outlet boundaries (Fig. 2c)) with a diameter of only 2.8 mm.

According to Calay et al. [4] the lung bifurcation should be discretized by about 100,000-150,000 cells per bifurcation. With a bifurcation number of 63 we receive a number of about 30,000 grid cells per bifurcation. Therefore an additional larger grid with 15 million cells (approx. 240,000 cells per bifurcation) is created for comparison.

### Characteristic flow parameters

The flow in the upper airways of the human lung can be defined by two non-dimensional characteristic numbers, the Womersley number  $\alpha$  and the Reynolds number  $Re$ . The Womersley number represents a non-dimensional frequency in oscillatory tube flow defined by the breathing frequency  $f$ , the kinematic viscosity  $\nu$  of the fluid and the diameter  $D$  of the trachea (equation 3).

$$\alpha_{trachea} = \frac{D}{2} \sqrt{\frac{2 \cdot \pi \cdot f}{\nu}}. \quad (3)$$

It describes the unsteady nature of fluid flow in response to an unsteady pressure gradient and is a ratio of

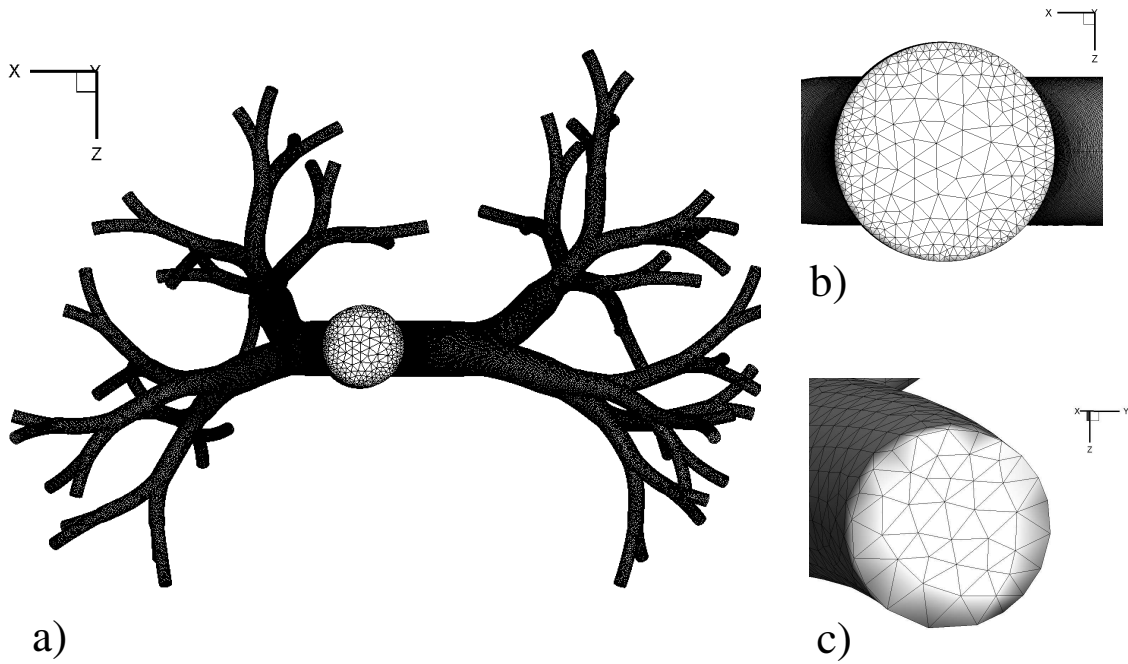


**Figure 2** Numerical grid structure of the lung model, a) complete lung model, b) enlarged view of the grid structure of the inlet boundary (top of the trachea), c) enlarged view of the grid structure of one of the outlet boundaries (distal end of the 6th generation).

inertia to viscous forces in oscillatory flows [24]. For very small Womersley numbers ( $\alpha < 3$ ), quasi-stationary flow can be assumed with velocity profiles similar to a laminar parabolic profile with the flow maximum in the pipe center [21]. For increasing  $\alpha$  the axial velocity profiles are no longer parabolic and the bulk flow is phase-shifted in time relative to the oscillating pressure gradient [21]. Consequently, the velocity maximum is shifted to the tube wall and the velocity profiles are characterized by an annular shape. In order to keep the Womersley numbers constant for the same geometric scale in model and original, the ratio of frequency to viscosity has to be kept constant.

The Reynolds number of the flow in the trachea indicates the laminar or turbulent character of the flow. It is defined as the ratio of inertia to viscous forces (equation 4).

$$Re_{trachea} = \frac{\rho U^2 A}{\eta \frac{U}{D}} = \frac{U \cdot D}{\nu}. \quad (4)$$

In equation 4  $\rho$  denotes the fluid density,  $\eta$  the dynamic viscosity,  $A$  is the cross section area,  $D$  the diameter of the trachea and  $U$  denotes the characteristic velocity which is the maximum of the mean axial velocity over the cross section of the trachea in this case. The maximum velocity depends on the tidal volume  $V$  and the oscillatory frequency  $f$  according to equation 7.

$$U = \frac{V}{2} \cdot \frac{2 \cdot \pi \cdot f}{A_{trachea}} = \frac{4 \cdot V \cdot f}{D^2}. \quad (5)$$

Hence, the Reynolds number can be written as

$$Re_{trachea} = \frac{4 \cdot V \cdot f}{D \cdot \nu}. \quad (6)$$

The characteristic flow parameters which were chosen for the subsequent study are summarized in Tab. 3.

**Table 3** Values of the characteristic flow parameters used for numerical flow analysis.

Frequency (Hz)	Tidal volume (ml)	Re	$\alpha$
0.15	500	2000	3.0
0.5	75	1000	5.5
1.5	75	3000	9.5

#### **Boundary and Starting conditions**

The linear set of equation can only be solved if both, starting and boundary conditions are available. The complete region of interest is initialized with zero pressure relative to the ambient pressure and zero velocity. For boundary conditions two different types of boundary conditions are used:

- Dirichlet boundary condition: a value of the variable is given
- Neumann boundary condition: a derivative of the variable is given

Boundary conditions had to specified for the inlet, the outlets and the wall, whereat the lung model contains one inlet and 64 outlets. The positions of the boundary conditions are depicted in Fig. 3.

The boundary conditions used for the simulation of the human lung flow are summarized in Tab. 4.

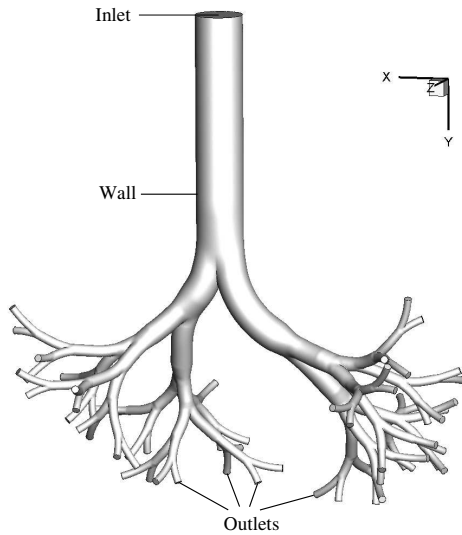


**Figure 3** Lung model with the positions of the boundary conditions.

**Table 4** Boundary conditions for the simulation of human lung flow.

Boundary	Variable	Condition	Type
Inlet	velocity $u$	$\underline{u} = \underline{u}_{max} \cdot \sin(\omega t)$	Dirichlet
	pressure $p$	$\underline{n} \cdot \nabla p = 0$	Neumann
Outlet	velocity $u$	$\underline{n} \cdot \nabla \underline{u} = 0$	Neumann
	pressure $p$	$p = 0$	Dirichlet
Wall	velocity $u$	$\underline{u} = 0$	Dirichlet
	pressure $p$	$\underline{n} \cdot \nabla p = 0$	Neumann

The values given in Tab. 4 apply perpendicular to the boundaries. The maximum velocity  $\underline{u}_{max}$  was determined according to the following equation

$$U_{max} = \frac{V}{2} \cdot \frac{2 \cdot \pi \cdot f}{A_{trachea}} = \frac{4 \cdot V \cdot f}{D^2}. \quad (7)$$

In equation 7  $V$  denotes the tidal volume,  $f$  is the ventilation frequency,  $A$  is the cross section area of the trachea and  $D$  denotes the diameter. The velocity was applied as uniform value at the inlet boundary. Therefore, the inflow tube (trachea) was lengthened to a total tube length of 20 cm in order to receive a more developed flow at the first model bifurcation. The original tube length of the model was 12 cm. According to Durst [6], the entrance length  $l$  to receive fully developed flow in a tube depends on the tube diameter  $D$  and the Reynolds number  $Re$ :

$$l = \left[ 0.619^{\frac{1}{6}} + (0.0567 Re)^{\frac{1}{6}} \right]^{\frac{1}{6}} D. \quad (8)$$

Equation 8 is valid for laminar pipe flow in the range of  $0 < Re < \infty$  [6]. For a Reynolds number of  $Re = 2000$  and a tube diameter of 18 mm an entrance length of 22 cm would be necessary to receive fully developed flow. Hence,

the tube length of the trachea in the numerical model represents a very good compromise between reliable results and numerical effort due to a large geometry, which needs to be discretized.

The numerical simulations were performed on the PC Farm Deimos of the ZIH (Center for Information Services and High Performance Computing) at the Technische Universität Dresden. Altogether, Deimos consists of 2576 processor cores [12] of which 64 were used. The time step size was varied between  $10^{-4}$  s and  $5 \cdot 10^{-4}$  s depending on the oscillatory frequency of the lung flow. With this time step size the average duration of the calculation of one period is about 48 h.

## Validation of the numerical results

### Comparison of different mesh size solutions

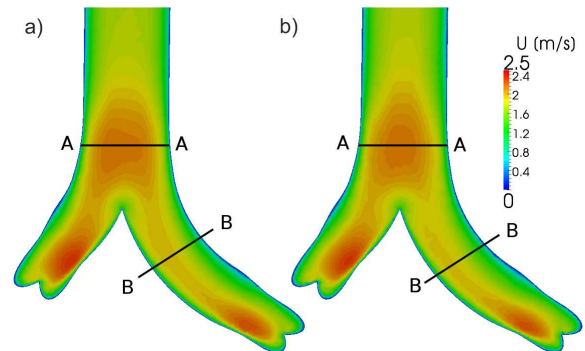


**Figure 4** Contours of velocity magnitude in a center cut through the main bifurcation of a) a 15 million cell tetrahedral grid and b) a 2 million cell tetrahedral grid. Locations of the cut sections A-A and B-B are added for reference.

As reported by Calay et al. [4]), the spatial resolution of the grid used is critical for accurate results. Hence, a 15 million cell tetrahedral grid is used to repeat one of the presented simulations. The structure of the mesh and its boundaries are identical to the 2 million cell mesh shown in 2. The additional cells are distributed evenly in the computational domain in order to enhance the spatial resolution of the inner part of the trachea and the lower branches. The starting solution for the computations with the 15 million cell grid is interpolated from the 2 million cell grid and therefore almost identical. The timestep size is adjusted with respect to a constant Courant number  $Co$  of 0.2 for both cases. In equation 9,  $\bar{u}$  denotes the velocity magnitude in the cell,  $\Delta t$  is the timestep size and  $\Delta l$  the cell length in the direction of the flow. The value of 0.2 is chosen due to stability reasons caused by the oscillating inlet boundary condition.

$$Co = \frac{\bar{u} \Delta t}{\Delta l} \quad (9)$$

Figure 4 shows the contours of the velocity magnitude in a center cut through the main bifurcation of a) the 15

million cell tetrahedral grid and b) the 2 million cell tetrahedral grid. The direct comparison shows that the principal features of the flow before and after the bifurcation are in good agreement. The velocity magnitude in both cases is nearly identical. Since the wall resolution of the 2 million cell grid is sufficient, no differences are to be expected to the 15 million cell grid near the walls.

Differences between the presented velocity fields are obvious in the center of the flow before the first bifurcation. Here the flow field of the 15 million cell grid shows an asymmetry with higher velocities on the left side. This asymmetry is not visible on the 2 million cell grid due to the coarse spatial resolution. Another obvious difference is the influence of the coarse spatial resolution in the lower right part of both pictures. Here the improved spatial resolution in figure 4 a) leads to more visible flow details.

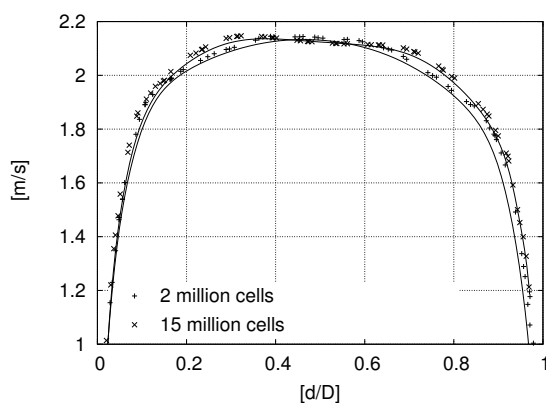


Figure 5 Velocity profiles in section A-A for the 2 (+) and the 15 (x) million cell grids

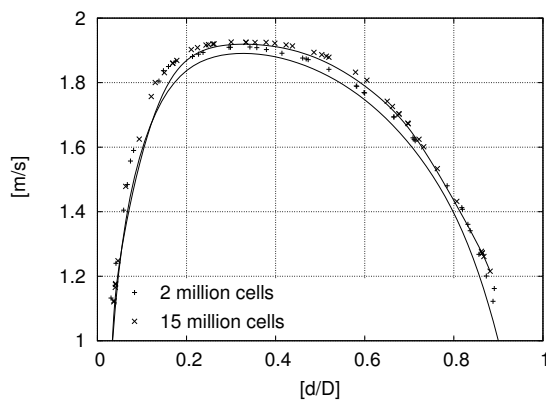


Figure 6 Velocity profiles in section B-B for the 2 (+) and the 15 (x) million cell grids

Since there are 2 regions with visible differences, those regions were sampled and compared in detail. Figures 4 a) and b) show black sample lines which are normal to the vector of the mean velocity. Figures 5 and 6 show the velocity profiles on these lines over a dimensionless diameter  $d/D$  in  $m/s$ . In the figures, + represents the sampled values of the 2 million cell grid and  $x$  denotes the values for

the 15 million cell grid, the solid lines represent curve fits through the discrete points. In figure 5 it is obvious, that the difference in the absolute values of the velocity magnitude is minimal. The asymmetry visible in figure 4 can be seen here as well. The profile of the 15 million cell grid is asymmetric and slightly m-shaped. In general, both profiles are in good agreement, although 15 million cell grid shows more details of the flow. Figure 6 shows the velocity profile in section B-B. The principal shape of the profile and the velocity magnitude are almost identical. Again minimal differences between the two profiles are visible. Nevertheless both are again in good agreement.

In summary, the investigation of the influence of the spatial resolution shows that the solution from 2 million cell grid is accurate enough for the problem. All the principal flow features known from literature and the experiment are evident. Although the 15 million cell grid shows more details of the flow it is reasonable to assume that the 2 million cell grid is fine enough to investigate variations of the boundary conditions in the order of magnitude used in this investigation. Due to the long computation times (approx 6 weeks on 256 cores) the other presented cases are solutions from the 2 million cell grid.

#### Validation of the numerical results

For validation of the numerical code, a comparison to experimental PIV-results of the first bifurcation is given. The experiments were carried out by Adler and Brücker [1]. First, the case of normal breathing under rest condition is chosen. The Reynolds number is  $Re = 2000$ , the Womersley number is  $\alpha = 3$  (compare Tab. ??). Figs. 7 and 8 depict the velocity contours and profiles in the center plane of the main branches for inspiration and expiration, respectively.

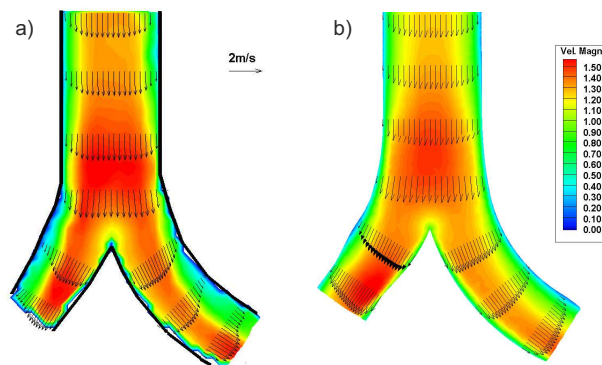
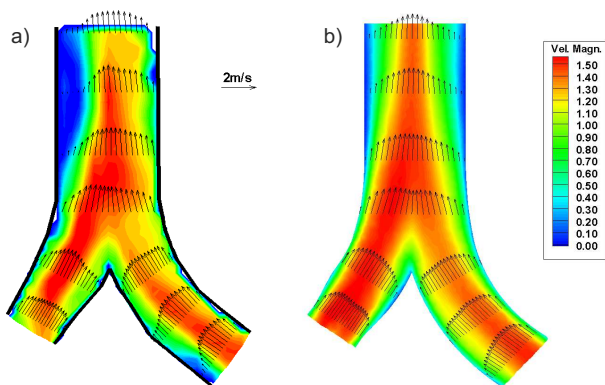


Figure 7 Velocity contours and profiles during peak inspiration, PIV - results (a), numerical results (b),  $Re = 2000$ ,  $\alpha = 3$ .

The comparison of inspiration shows good agreement of PIV-measurements and numerical results (Fig. 7). The regions of high velocity have similar extensions. During inspiration the acceleration of the flow ahead of the bifurcation is found in both cases. A small deviation occurs for the velocity profiles which have higher gradients near the



**Figure 8 Velocity contours and profiles during peak expiration, PIV - results (a), numerical results (b),  $Re = 2000$ ,  $\alpha = 3$ .**

wall in the PIV - measurements. A possible explanation could be the numerical grid, which might be too coarse to fully resolve the Stokes boundary layer, especially in the lower branches. Furthermore, the peak velocity at the top of the trachea is higher than in the numerical calculation, probably due to a shorter entrance length of the numerical model.

During expiration (Fig. 8) the numerical and experimental results are still in acceptable agreement. The velocity is in a similar range for both cases and the velocity profiles are characterized by a comparable asymmetry.

The PIV-measurements suggest a separation region in the trachea which does not occur in the numerical calculation. However, this separation region was only observed experimentally for this single case of  $Re$  and  $\alpha$  given above. Therefore, it is not assumed to be typical for the flow in the lung model and the numerical data should be correct for this case.

The cross sectional flow is compared for one case of high frequency ventilation with  $Re = 1000$  and  $\alpha = 5.5$ . Fig. 9 shows the flow patterns in a cross section of the trachea during maximum expiration. Fig. 9 a) presents the experimental result, Fig. 9 b) the numerical result, whereat the color coded contour of the vorticity is superposed with the cross sectional stream lines.

Qualitatively as well as quantitatively there is a good agreement between both results. The double vortex pair occurs in both cases at even similar strength. The vortex structure of the numerical simulation is more symmetric than the experimental result and the vortex shapes vary slightly.

To conclude, based on the validation results, the numerical simulation can be used to predict the flow behavior in regions, at which experimental data are not available. There are small deviations concerning the velocity profiles in the first daughter branch. These can have different reasons. First, the numerical grid is quite coarse considering the cross sectional resolution of the flow. Thereby, small structures were probably not fully resolved. Sec-

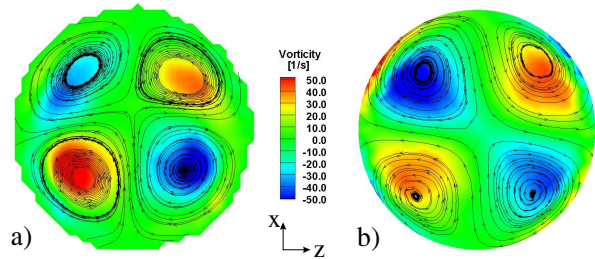


**Figure 9 Vorticity contours, color coded, where blue indicates clockwise (negative) and red counterclockwise (positive) sense of rotation, respectively, superposed are cross sectional streamlines,  $Re = 1000$ ,  $\alpha = 5.5$ , (a) PIV - results, (b) numerical results.**

ond, the size of the interrogation areas, chosen for the PIV-evaluation, also determines the resolution of the experimental results. Here, the distance of two grid points was about 1.1 mm. Hence, the trachea was resolved by approximately 16 grid points. Since this resolution is also quite coarse, it is possible that small flow details are not resolved due to the averaging of the velocity field across one interrogation area. Nevertheless, both, experimental and numerical results are in good agreement with results from other researchers presented in the literature, e.g. [4, 5, 8, 14, 15, 19] and typical flow phenomena could be shown. Therefore the validated numerical model can be used for further investigations.

## Numerical results

Numerical results are given for the velocity distribution by iso-surfaces of the velocity magnitude. Fig. 10 shows the surface of constant velocity vector magnitude of  $0.95m/s$  for peak inspiration (a) and peak expiration (b) during normal breathing.

During inspiration, the velocity seems to increase from the trachea down to the 3rd generation as marked by the increasing area which is occupied by the iso-surface (Fig. 10a)). This can be explained by the slightly decreasing total cross section area down to this generation. Ahead of each bifurcation, a further increase of velocity occurs, which is also caused by the contraction of the flow at this point. The orientation of the iso-surface changes strongly from generation to generation. The fluid is always pushed to the outer walls of the curvature as already found in the experiments. The distribution between left and right main branch is asymmetric which is obviously a consequence of the smaller curvature radius of the right main branch and hence, a higher pressure loss.

At the first glance, the iso-surfaces of the same velocity during expiration show a similar distribution as for inspiration (Fig. 10b)). Even these branches of the 4th generation which were characterized by higher velocities during inspiration show enlarged contour surfaces during expiration. This means that the pressure loss difference between the branches is the same for inspiration and expiration.

However, a closer look at the iso-surfaces reveals their

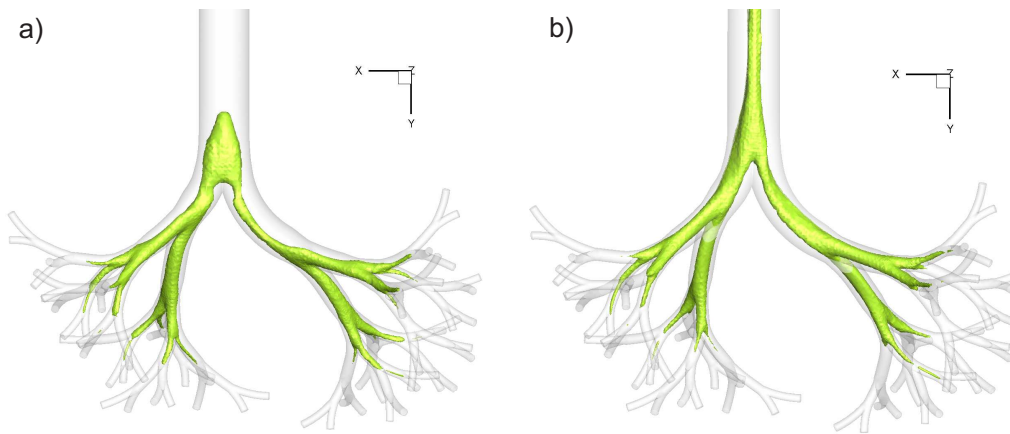


**Figure 10 Iso-contours of the velocity magnitude for  $0.95\text{m/s}$  for peak inspiration (a) and peak expiration (b),  $Re = 2000$ ,  $\alpha = 3$ , the complete lung geometry is superposed.**

different shape during inspiration and expiration. During inspiration, the contours are curved following the branch geometry, while during expiration, the contours appear to run straight through the branches. As already observed in the experiments, the location of the same velocity contour has shifted. Additionally, the three-dimensional shapes of the iso-surfaces have changed. In the left branch of the first generation the surface has the largest extension in  $z$ -direction (during inspiration). In the trachea, the maximum extension of the iso-surface occurs in the  $x$ - $y$ -plane. In contrast, during expiration, the directions of the maximum extension are twisted. In the first generation, the maximum extension occurs in the  $x$ - $y$ -plane, in the trachea, it occurs in the perpendicular  $y$ - $z$ -plane.

The transitions from expiration to inspiration and from inspiration to expiration are shown in Fig. 11 a) and b), respectively. The figures represent the iso-contours of the  $y$ -velocity, where red contours mark positive flow direction (downwards into the lung), while blue contours mark negative flow direction (upwards). The phase shift of the flow during the transition times can be clearly seen. Fig. 11 reveals a characteristic structure of the transition zones. Typically, the return of the flow is initiated in the low inertia zones, in particular, zones of lower velocities. During change from expiration to inspiration (Fig. 11a) two pairs of characteristic zones emerge in the trachea. On the left and right sides, the flow is directed into the model (red structure), i.e. the inspiration has already started, whereas at the front (anterior) and rear (posterior) center of the trachea, expiration (blue structure) still takes place. A comparison to the iso-contour during maximum expiration reveals that the maximum flow velocity occurs in the  $y$ - $z$ -plane. Hence, the plane of lower inertia flow is the  $x$ - $y$ -plane in which the change of flow direction is initiated.

During change from inspiration to expiration (Fig. 11b)) the flow structure is completely different. The core flow is still directed into the lung, whereas at the wall an annulus of fluid is already directed upwards.

Considering the secondary flows in a realistic lung

geometry, their structure varies strongly even within one branch. Experimentally, the flow in two selected planes in the trachea and left branch of the first generation was analysed and presented above. It was assumed that these secondary flow structures are representative for the selected branches. Now, as numerical data are available, the secondary flow structure can be visualized in the complete model. Fig. 12 shows the iso-contours of the helicity for peak inspiration and expiration for normal breathing. The helicity is a measure for the strength of helical structures. It is defined by

$$H = \underline{u}(\nabla \times \underline{u}), \quad (10)$$

whereat a scalar value is received. Color coded, the helicity represents the different senses of rotation, i.e. red - positive, clockwise rotation, blue - negative, counterclockwise rotation and the shape of the helical vortices can be seen.

During inspiration (Fig. 12 a), a vortex pair, can be found in each generation of the model. The extension of the vortex pair is maximal at the beginning of each generation and decreases slightly at the end. The helicity magnitude is preserved again down to the 3rd generation and decreases slightly further downstream, which can be seen from the smaller iso-contour surfaces. Consequently, it is assumed that the secondary vortices scale with the local velocity which remains constant down to the 3rd generation.

During expiration, the PIV results presented by Adler and Brücker [1], have shown a double vortex pair in the trachea. This structure was not observed in the first branch. Now, the complete structure of the vortex generation in the whole model can be visualized (Fig. 12 b). It can be seen that the double vortex pair starts to form upstream at each bifurcation originating from a single vortex pair which approaches from the two daughter branches. Further upstream, the double vortex pair vanishes due to the influence of the curvature of the branches. Hence, a new

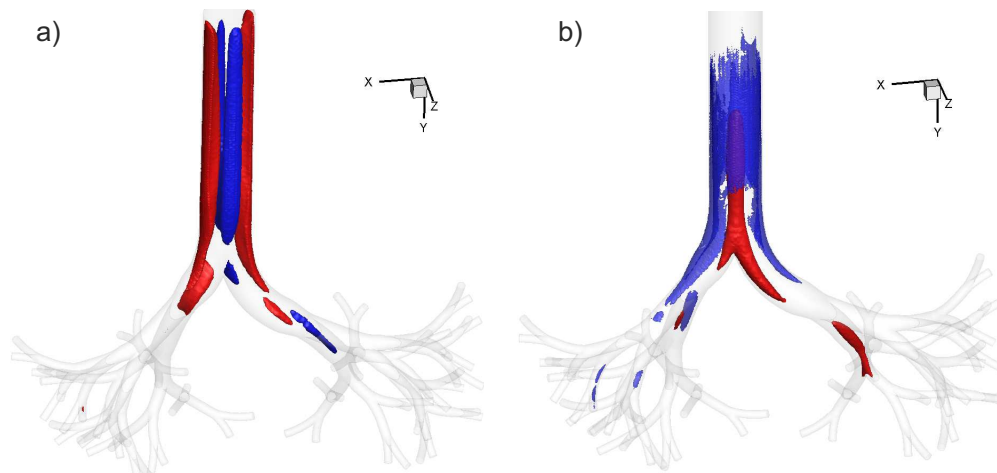


**Figure 11 Iso-contours of the y-velocity during transition from expiration to inspiration (a) and from inspiration to expiration (b), red and blue color indicates positive and negative velocity in the y-direction, respectively.**

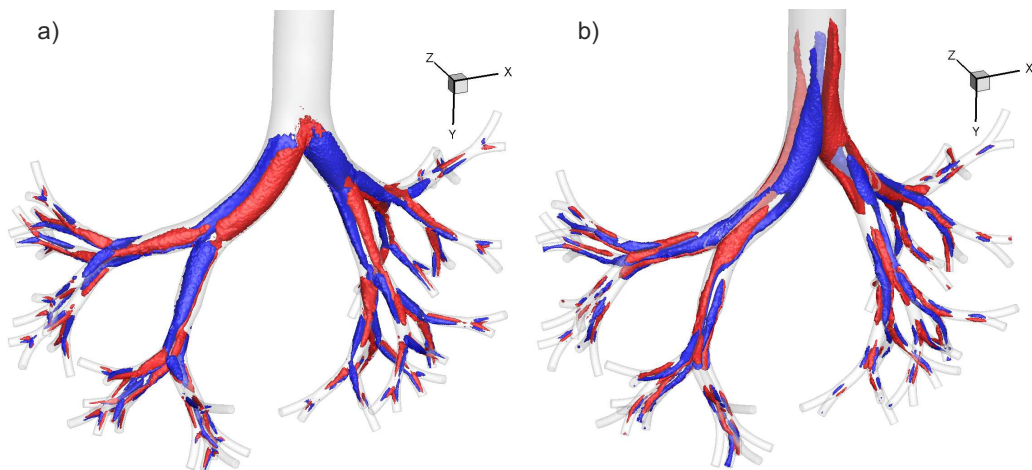


**Figure 12 Iso-contours of the helicity during peak inspiration (a) and expiration (b), red indicates positive, clockwise rotation, blue - negative, counterclockwise rotation.**

vortex pair is generated at the outside of the bend. As no curvature exists, which is the case in the trachea, the vortex only loses strength. The maximum secondary velocity found here is about 20% of the average main flow velocity, which is in agreement with Ref. [9].

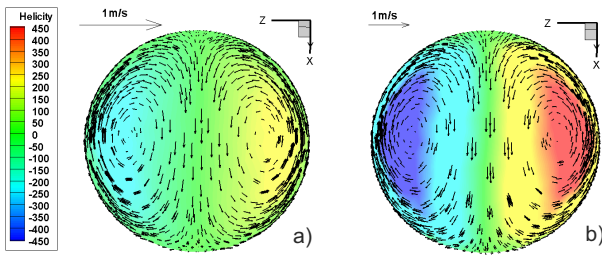


**Figure 13** Velocity vectors and contour of the helicity in a cross section of generation 1 for two different Reynolds numbers, a)  $Re = 2000$ , b)  $Re = 3000$ .

To confirm the assumption that the vortices scale with the local main velocity, i.e. Reynolds number, the velocity vectors in combination with the helicity contours are illustrated in Fig. 13 for two different Reynolds numbers,  $Re = 2000$  (Fig. 13 a) and  $Re = 3000$  (Fig. 13 b). Each image shows the same cross section of the first generation (upper cross section in Fig. 14). It can be seen that for  $Re = 3000$  the helicity is about three times higher than for  $Re = 2000$ . The in-plane velocity has approximately doubled. This means that secondary vortex strength strongly increases with higher  $Re$  and the relation is not linear. These findings are in contrast to Fresconi and Prasad [9] who stated that up to a critical Reynolds number of  $Re = 100$ , secondary vortex strength increases linearly with  $Re$  and above this number, the vortex strength remains nearly constant.

In order to gain more information about the vortex structure, different planes of the first and second generation are selected and the in-plane streamlines are plotted (Fig. 14). At the beginning of each branch the vortex pair is symmetric and well pronounced, the strength is maximal. Further downstream, it loses strength and the characteristic symmetric vortex pair vanishes. The sectional streamlines rather indicate a single swirl. At the bifurcation, two new vortex pairs start to emerge.

These numerical results show that structure of the secondary vortices strongly varies along the branch. Hence, the experimental measurements were apparently carried out in a plane in which the vortex structure has vanished. This finding is in contrast to Fresconi and Prasad [9] who assumed a constant vortex structure throughout the complete branch.

The validated numerical model allows not only the investigation of the lower generations of the lung, it allows the comparison of varied boundary conditions. Figure 15 depicts a comparison between the Womersley numbers of  $\alpha = 5.5$  and  $\alpha = 9.5$  at the time when the principal flow direction at the inlet is zero and changes direction from ex-

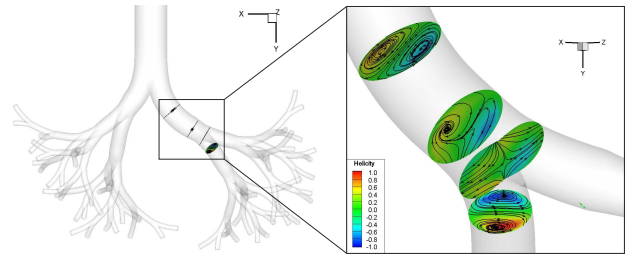


**Figure 14** Secondary flow structures in selected cross section of the right main branch, color contours represent the helicity, superposed are in-plane streamlines.

piration to inspiration. Due to the different frequencies the maximum velocity magnitude for both cases is different. But it is mentionable that the location of the maximum is shifted from the center to the wall, especially in the mother branch. In the daughter branches the flow pattern is asymmetric for  $\alpha = 9.5$ . This indicates a phase shift between adjacent branches and leads to pendelluft. The curved arrow in figure 15b) indicates the location of this effect.

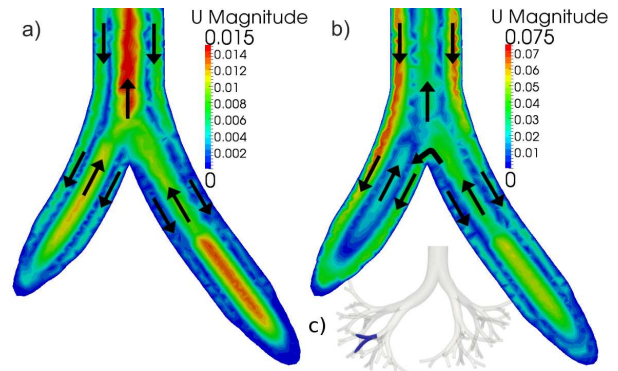


**Figure 15** Velocity magnitude in a cut through the 5th generation for two different Womersley numbers but the same tidal volumes of  $TV = 75\text{ml}$ : a)  $\alpha = 5.5$  b)  $\alpha = 9.5$ . Black arrows indicate flow direction. c) Location of the cut in the lung.

## Conclusions

The numerical simulation is in good agreement with the experimental results and the investigation of the grid influence shows that the used spatial resolution is sufficient. Hence, flow phenomena which could not be measured can now be visualized by using the according numerical data. At the times of flow transitions from ex- to inspiration and ins- to expiration, the flow is bidirectional due to the phase shift of oscillatory flow; characteristic regions with different flow directions develop. These regions reflect the different flow structure during ins- and expiration. Since during expiration the maximum flow velocity occurs in the  $y-z$ -plane in the center of the tube, the return of the flow has to be initiated at the outside of the perpendicular  $x-y$ -plane. During inspiration such a characteristic plane of maximum velocity does not develop. Hence, the flow starts turning

annularly close to the wall. Furthermore, it could be shown that vortical structures occur in all generations during inspiration and expiration. Vortex pairs are generated during inspiration in each branch by centrifugal forces. Due to the change in curvature and bifurcating geometry, vortex pairs are not conserved beyond a bifurcation but rather develop anew. In contrast, the vortex pairs from the daughter branches unite in the parent branch to two vortex pairs during expiration. However, halfway through the tube the vortex pairs have vanished and start to develop again. Consequently, the flow structure depends on the local curvature and does not have a history from the upstream flow.

## Acknowledgements

The authors gratefully acknowledge the Center for Information Services and High Performance Computing of the TU Dresden, Germany for allocating the computer time to perform the simulation. This project was supported by the Deutsche Forschungsgemeinschaft, grant No. BR 1494/7-1.

## References

- [1] K. Adler and C. Bruecker. Dynamic flow in a realistic model of the upper human lung airways. *Experiments in Fluids*, 43(2-3):411–423, 2007.
- [2] K. Bauer, H. Chaves, and C. Bruecker. Visualizing flow partitioning in a model of the upper human lung airways. *Journal of Biomechanical Engineering*, 132(3), 2010.
- [3] T. Behrens. Openfoam's basic solvers for linear systems of equations. [http://www.tfd.chalmers.se/~hani/kurser/OS\\_CFD\\_2008/TimBehrens/tibeh-report-fin.pdf](http://www.tfd.chalmers.se/~hani/kurser/OS_CFD_2008/TimBehrens/tibeh-report-fin.pdf), 2009.
- [4] R. Calay, J. Kurujareon, and A. Holdo. Numerical simulation of respiratory flow patterns within human lung. *Respiration Physiology*, 130:201–221, 2002.
- [5] C. Dragon and J. B. Grotberg. Oscillatory flow and mass transport in a flexible tube. *Journal of Fluid Mechanics*, 231:135–155, 1991.
- [6] F. Durst, S. Ray, B. ĀIInsal, and O. Bayoumi. The development lengths of laminar pipe and channel flows. *Journal of Fluids Engineering*, 127 (6):1154–1161, 2005.
- [7] A. Farag, J. Hammersley, D. Olson, and T. Ng. Mechanics of the flow in the small and middle human airways. *Journal of Fluids Engineering, Transactions of the ASME*, 122(3):576–584, 2000.
- [8] F. Fresconi and A. Prasad. Flow and convective dispersion in the conductive airways of the human lung. pages 101–102, 2007.
- [9] F. Fresconi and A. Prasad. Secondary velocity fields in the conducting airways of the human lung. *Journal of Biomechanical Engineering*, 129(5):722–732, 2007.
- [10] B. Heraty, J. Laffey, and N. Quinlan. Fluid dynamics of gas exchange in high-frequency oscillatory ventilation: In vitro investigations in idealized and anatomically realistic airway bifurcation models. *Annals of Biomedical Engineering*, 36 (11):1856–1869, 2008.
- [11] K. Horsfield, G. Dart, D. Olson, G. Filley, and G. Cumming. Models of the human bronchial tree. *Journal of applied physiology*, 31(2):207–217, 1971.
- [12] G. Juckeland. [http://tu-dresden.de/die\\_tu\\_dresden/zentrale\\_einrichtungen/zih/hpc/hochleistungsrechner/deimos](http://tu-dresden.de/die_tu_dresden/zentrale_einrichtungen/zih/hpc/hochleistungsrechner/deimos), 16.08. 2010.
- [13] C. Kleinstreuer, Z. Zhang, and Z. Li. Modeling air-flow and particle transport/deposition in pulmonary airways. *Respiratory Physiology and Neurobiology*, 163(1-3):128–138, 2008.
- [14] W. Lee, M. Kawahashi, and H. Hirahara. Experimental analysis of air flows in bronchial airway models in the cases of natural breathing and hfov. *Journal of Fluid Science and Technology*, 1(2):82–93, 2006.
- [15] W. Lee, M. Kawahashi, and H. Hirahara. Experimental analysis of pendelluft flow generated by hfov in a human airway model. *Physiological Measurement*, 27(8):661–674, 2006.
- [16] B. Lieber and Y. Zhao. Oscillatory flow in a symmetric bifurcation airway model. *Annals of Biomedical Engineering*, 26(5):821–830, 1998.
- [17] Y. Liu, R. So, and C. Zhang. Modeling the bifurcating flow in an asymmetric human lung airway. *Journal of Biomechanics*, 36:951–959, 2003.
- [18] N. Nowak, P. Kakade, and A. Annapragada. Computational fluid dynamics simulation of airflow and aerosol deposition in human lungs. *Annals of Biomedical Engineering*, 31(4):374–390, 2003.
- [19] A. Ramuzat and M. Riethmuller. Piv investigations of oscillating flows within a 3d lung multiple bifurcation model. *11th Int. Symp. On Appl. of Laser Techniques to Fluid Flows, Lisbon, Portugal*, paper 19-1, 2002.
- [20] J. Tarbell, J. Ultman, and L. Durlofsky. Oscillatory convective dispersion in a branching tube network. *Journal of Biomechanical Engineering*, 104(4):338–342, 1982.
- [21] S. Uchida. The pulsating viscous flow superposed on the steady laminar motion of incompressible fluid in a circular pipe. *ZAMP*, 7:403–422, 1956.
- [22] H. Versteeg and W. Malalaskera. *An Introduction to Computational Fluid Dynamics*. Pearson Education Limited, 2nd edition, 2007.
- [23] E. Weibel. *Morphometry of the human lung*. Springer-Verlag, 1963.
- [24] J. Womersley. Method For The Calculation Of Velocity, Rate Of Flow And Viscous Drag In Arteries When The Pressure Gradient Is Known. *Journal Of Physiology-london*, 127(3):553–563, 1955.
- [25] Z. Zhang and C. Kleinstreuer. Airflow structures and nano-particle deposition in a human upper airway model. *Journal of Computational Physics*, 198:178–210, 2004.